# Impact of Inner Control in GFM-Induced Sub-Synchronous Oscillations

Muhammad Sharjeel Javaid *Student Member, IEEE*, Balarko Chaudhuri *Fellow, IEEE*, Fei Teng *Senior Member, IEEE*, and Zohaib Akhtar *Senior Member, IEEE*

***Abstract*—In power systems dominated by grid-forming inverters (GFMs), strong grid conditions can lead to sub-synchronous oscillations (SSOs) due to the reduced time-scale separation between GFM control loops and network dynamics, potentially causing instability. Modal analysis reveals that states associated with inner control (comprising current and voltage control loops) and network dynamics are the primary contributors to these oscillatory modes. This paper provides an analytical explanation of adverse interactions between GFM inner control and network dynamics that lead to SSOs. Through damping ratio sensitivity analysis, we establish that increasing the current control closed-loop bandwidth and the voltage control proportional gain can effectively mitigate these oscillations. The proposed control adjustments also prove effective in larger systems with 100% inverter-based resources penetration, comprising of a mix of both grid-following and grid-forming inverters.**

***Index Terms*—Grid-forming inverter, modal analysis, small-signal stability, sub-synchronous oscillation.**

## I. Introduction

The transition to renewable energy has led to an increasing dominance of inverter-based resources (IBRs) in power systems, replacing conventional synchronous generators [1]. Among IBR control strategies, grid-following inverters (GFLs) are widely used but face stability challenges, particularly in weak grids [2]. Grid-forming inverters (GFMs), in contrast, offer improved stability in weak-grid conditions and enable standalone operation [3], making them a promising solution for future power systems.

In GFMs, active and reactive power controllers determine the voltage magnitude and angle at the point of common coupling (PCC) [4]. While much attention has been given to the primary control design (e.g., droop control [5] and virtual synchronous generator (VSG) control [6]), this work focuses on the impact of inner control–the voltage and current control. Their control gains are typically tuned locally. Current control is tuned using pole-zero cancellation [7] and voltage control is generally tuned using symmetrical optimum (SO) [8]. The voltage control design method, in particular, assumes idealized conditions, such as high current control bandwidth and resistive networks [9], which do not hold in practical high-power applications where switching frequency limitations impose constraints on bandwidth [10].

Several studies have investigated the sensitivity of eigenvalues to IBR control parameter variations, primarily relying on linearized numerical models. For GFL, such studies are conducted in [11], [12], [13]. Similarly, for GFMs, [14], [15] have employed numerical models to study control interactions, but analytical insights into the underlying mechanisms remain largely unexplored. Such approaches offer limited explanation on the fundamental interactions that drive sub-synchronous oscillations (SSOs). This paper addresses this gap by presenting an analytical formulation of a simplified GFM model, focusing on inner control dynamics. The analysis proposes two key mitigation strategies–increasing voltage control proportional gain or current control bandwidth–to enhance system stability. These analytical insights align with prior numerical observations and are also validated on a large-scale 100% IBR-driven system. This paper reveals that modal participation patterns remain similar across variations in voltage control gains, current control bandwidth, and network strength, making it difficult to diagnose the exact source of SSOs using eigenvalue-based methods alone. Our findings also highlight the need to incorporate network dynamics into control design.

This work was supported in part by Punjab Educational Endowment Fund, Pakistan and the Engineering and Physical Science Research Council, UK [grant number EP/Y025946/1]. Data supporting this study are available at GitHub link Any queries about the data could be sent to the EPICS UK project administrator g.eroglu@imperial.ac.uk

## II. Grid-forming Inverter Dynamic Model

GFM is modeled in its local $dq$ rotating reference frames. The current or voltage $(X)$ in local $dq$ frame is transformed onto a common network reference frame $DQ$ using $X_{DQ} = X_{dq}e^{j\theta}$ where $\theta$ is the angle between the two frames. The aggregated model of the GFM is shown in Fig. 1 with the grid-side converter equipped with an $LC$ filter, as in [16]. The dynamics of the primary resource (wind turbine, solar panel, etc.) is not considered to keep the study resource agnostic. As the focus of this paper is small-signal stability, we assume balanced operation and narrow-band signals tightly centered around the nominal frequency.

The complete GFM model block diagram is shown in Fig. 2 and the corresponding state equations are given in (1).

$$\dot{x}_d = (\Delta I_{d_r} - x_d K_{I_d})/K_{P_d} = V_r - V_d \tag{1a}$$
$$\dot{x}_q = (\Delta I_{q_r} - x_q K_{I_q})/K_{P_q} = 0 - V_q \tag{1b}$$
$$\dot{I}_{d_i} = (I_{d_r} - I_{d_i})/\tau_c \tag{1c}$$
$$\dot{I}_{q_i} = (I_{q_r} - I_{q_i})/\tau_c \tag{1d}$$
$$\dot{\theta} = D_{P\omega}(P_r - P_m) = \Delta\omega \tag{1e}$$
$$\dot{P}_m = (V_d I_d + V_q I_q - P_m)/\tau_m \tag{1f}$$
$$\dot{V}_d = (I_{d_i} - I_d)/C_f + \omega V_q \tag{1g}$$
$$\dot{V}_q = (I_{q_i} - I_q)/C_f - \omega V_d \tag{1h}$$

From the block diagrams of Fig. 2, following algebraic equations directly follow:

$$I_{d_r} = \omega C_f V_q + \Delta I_{d_r} - I_d \tag{2a}$$
$$I_{q_r} = \omega C_f V_d + \Delta I_{q_r} + I_q \tag{2b}$$

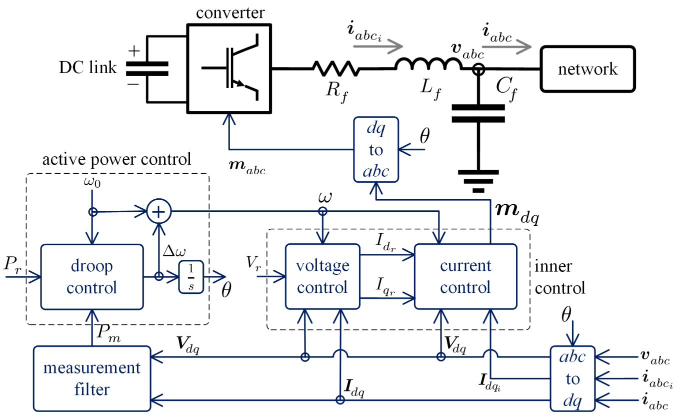


Fig. 1. Control blocks for a GFM with an LC filter.

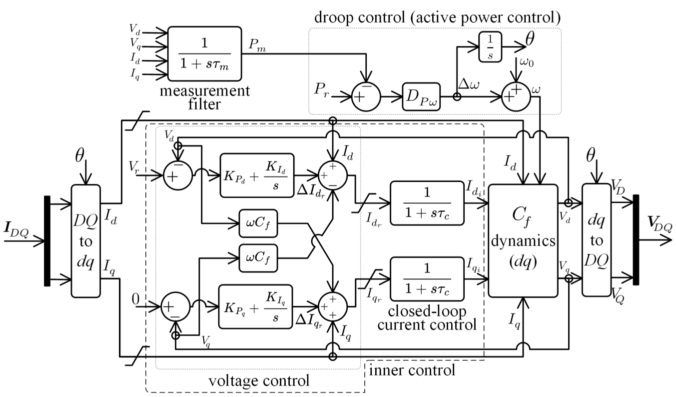


Fig. 2. GFM model block diagram.

In the inner control, the voltage control sets the current references, $I_{dq_r}$ (see (1a), (1b) and (2a), (2b)). Here, $x_d$ and $x_q$ denote PI control states of voltage control. Considering perfect decoupling feed-forward [7], the closed-loop current control is simplified to a first-order time lag with a specified bandwidth ($\equiv 1/(2\pi\tau_c)$ Hz), governed by (1c), (1d). In secondary control, only active power frequency droop control (1e) with a specified measurement filter (1f) of bandwidth ($\equiv 1/(2\pi\tau_m)$ Hz) is employed that sets the angle and frequency of the voltage at PCC. Equations (1g) and (1h) characterize the dynamics of the filter capacitor. Reactive power-voltage droop is not implemented, allowing the voltage magnitude reference to remain independent of reactive power.

The voltage control gains of a GFM are tuned using the SO method [7], [17]. Notably, the design in the SO method is carried out locally using only GFM parameters. This means that the SO method does not account for the static or dynamic strength of the network at the PCC. Assuming $I_{dq}$ is independent of the network and $\tau_c$ is very small, the gain crossover frequency $\omega_m$ determines the proportional and integral gains, denoted by $(K_{P_d}, K_{P_q})$ and $(K_{I_d}, K_{I_q})$, respectively, as below:

$$K_{P_d} = K_{P_q} = C_f\omega_m \tag{3}$$

$$K_{I_d} = K_{I_q} = \tau_c C_f \omega_m^3 \tag{4}$$

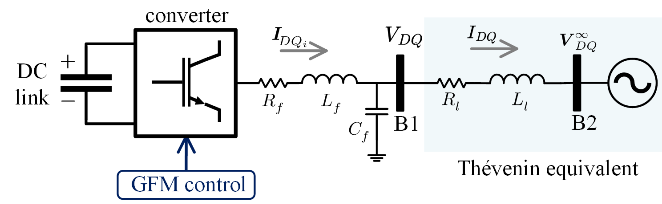


Fig. 3. A GFM connected to a Thévenin equivalent of a power system.

TABLE I
GFM PARAMETERS

| $K_{P_{dq}}$ | $K_{I_{dq}}$ | $\tau_c$ (ms) | $\tau_m$ (ms) | $D_{P\omega}$ | $\omega_0 C_f$ (pu) |
|---|---|---|---|---|---|
| 0.2 | 4.67 | 0.3 | 7.9 | 3.14 | 0.22 |

The frequency $\omega_m$ is proportional to the closed-loop bandwidth of the voltage control. Also, $\omega_m$ and $\tau_c$ are related to phase margin $\delta_m$: $\tau_c\omega_m = \sqrt{(1-\sin\delta_m)/(1+\sin\delta_m)}$

From (1), the dynamic model of GFM has 8 states, and 8 performance parameters ($K_{P_d}$, $K_{P_q}$, $K_{I_q}$, $K_{I_q}$, $\tau_c$, $C_f$, $\tau_m$, $D_{P\omega}$). Among these parameters, $\tau_m$ and $D_{P\omega}$ are held constant throughout this paper, set at $\tau_m = 7.9$ ms and $D_{P\omega} = 0.01 \cdot \omega_0 / P_{\text{rated}}$, as examining their influence is beyond the scope of this study. Here, $\omega_0$ represents the nominal system angular frequency ($\omega_0 = 2\pi \cdot 50$ rad/s).

## III. Small-Signal Analysis

This section explores the impact of interactions between GFM control and network states by analyzing a circuit in which the GFM is connected to a Thévenin equivalent of a power system, as shown in Fig. 3. The Thévenin equivalent is modeled in the common network $DQ$ frame such that $V_{DQ} = V_{dq}e^{j\theta}$, and $I_{DQ} = I_{dq}e^{j\theta}$. The dynamic equations of Thévenin equivalent of Fig. 3 are given below:

$$L_l \dot{I}_D = (V_D - V_D^\infty - I_D R_l) + \omega_0 L_l I_Q \tag{5}$$

$$L_l \dot{I}_Q = (V_Q - V_Q^\infty - I_Q R_l) - \omega_0 L_l I_D \tag{6}$$

A simple case with one IBR is chosen to eliminate the possibility of inter-GFM oscillations and focus exclusively on the interaction between the GFM and network states in SSO modes. This setup reflects a typical GFM connection compliance study, where the GFM vendor or developer must comply with connection requirements across a range of Thévenin equivalent impedances, representing both strong and weak grid scenarios.

In this analysis, the GFM exports 1.0 pu active power and maintains a 1.0 pu voltage at the PCC. The GFM performance parameters are tabulated in Table I. Due to simplifications in current control, the filter values of $R_f$ and $L_f$ are not explicitly required for small-signal analysis. However, for EMT (point-on-wave) validation studies (not shown in this work), an $R_f$ of 0.01 pu and $\omega_0 L_f$ of 0.2 pu has been used.

Figure. 4(a) examines the directional movement of the dominant SSO mode as three key parameters—SCR, $K_P$, and $\tau_c$—are varied. In this analysis, when one parameter is varied to its extreme value, indicated by black markers, the other

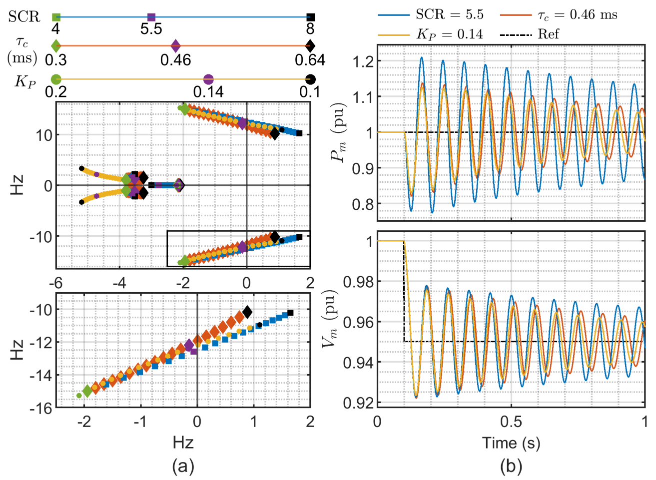


Fig. 4. For a GFM connected to a Thévenin equivalent: (a) SSO mode trajectories when the SCR is varied from 4 to 8 (square), $\tau_c$ is varied from 0.3 to 0.64 (diamond), and $K_{P_{dq}}$ is varied from 0.2 to 0.1 (circle); (b) active power and voltage reference tracking when the reference voltage is reduced to 0.95 pu at 0.1 s for three oscillatory scenarios, denoted by purple markers.

two parameters are held at their base values, denoted by green markers. The time constant $\tau_c$ and closed-loop bandwidth $f_c$ of the current controller are related by $\tau_c = 1/(2\pi f_c)$. The trajectories of the SSO modes are plotted as each parameter is varied: SCR (blue square markers), $\tau_c$ (red diamond markers), and $K_{P_{dq}}$ (orange circle markers). Across all three variations, these modes remain in close proximity, especially before reaching instability, suggesting that the dominant SSO mode responds in a similar manner to changes in each parameter.

Figure 4(b) shows the time-domain response (active power and voltage reference tracking) at the purple markers indicating conditions near the stability threshold for each parameter. These responses exhibit nearly identical frequencies and damping characteristics, making them practically indistinguishable. The critical stability points for each parameter are identified as follows: SCR at 5.5, $\tau_c$ at 0.46 ms, and $K_{P_{dq}}$ at 0.14. The droop gain remains constant across all three variations.

To further investigate the nature of this dominant SSO mode, centered around a frequency of approximately 12.5 Hz, its mode shapes are presented in Fig. 5. This modal analysis is conducted at the stability threshold for each parameter, as indicated by the purple markers in Fig. 4(a). The magnitude of the participation factor is represented by the size of the markers, while the angle of the markers reflects the mode shapes. This visual representation allows us to examine both the participation and the oscillation pathways simultaneously. The markers are color-coded to distinguish the contributions from different states: blue for network states ($I_D$, $I_Q$), red for current control ($I_{d_i}$, $I_{q_i}$), yellow for voltage control ($x_d$, $x_q$), and gray for other states ($V_d, V_q, P_m, \theta$).

The results indicate that, although the SSO mode is caused by variation in different parameters, the mode shapes and participation factors remain consistent. The similarity in the mode shapes of Fig. 5 implies that mode shape analysis alone is insufficient to pinpoint which specific parameter variation is causing the oscillation. This insufficiency highlights

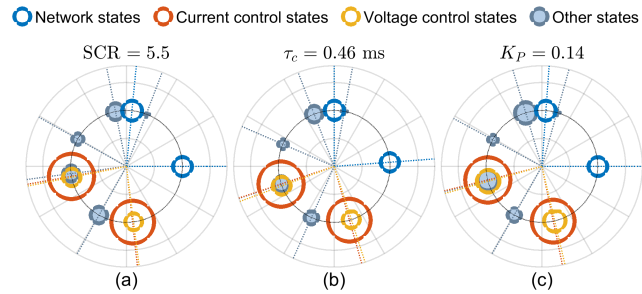


Fig. 5. Mode shapes representing the signature of the oscillatory mode (∼12.5 Hz) when (a) SCR = 5.4; (b) $\tau_c$ = 0.46 ms; (c) $K_P = 0.14$.

a limitation in using modal analysis as the sole diagnostic tool for identifying the source of oscillation within a GFM. Moreover, since modal analysis reveals minimal participation from the state associated with the power droop loop $(P_m)$, it is reasonable to conclude that for lower bandwidths of $P$-control (in this case, 0.96 Hz), the oscillation pathway observed in Fig. 5 will remain largely unchanged, regardless of the specific control structure (droop, VSG, etc.).

The small-signal analysis of the GFM-Thévenin equivalent system has demonstrated how variations in network and control parameters can drive the system toward instability. The conclusions drawn here are not intended to capture transient or large-signal behaviors because such events involve nonlinear dynamics and saturation effects, which extend beyond the applicability of the small perturbation assumption. A simplified GFM model, presented in the next section, allows us to analytically examine the sensitivity of system damping to inner control parameters.

## IV. Inner Control Sensitivity Analysis

To gain deeper insights into the specific influence of inner control parameters on system damping, this section simplifies the GFM model and focuses on the sensitivity analysis of its inner control dynamics.

The participation of $dq$ states is similar in SSO mode, as shown by the consistent marker sizes for network, current control, and voltage control in Fig. 5. This similarity indicates that the $dq$ axes are reasonably decoupled. Therefore, either of the axes can represent the impact of inner control on SSO mode. This analysis also excludes droop control, as these oscillations arise predominantly from interactions between inner control and network states, with minimal droop control participation. For brevity, the subscripts and superscripts for all parameters and variables are also removed.

Figure 6 illustrates the step-by-step process leading to simplified GFM dynamic model. It begins with a representation of the GFM as a voltage source with an $LC$ filter (Fig. 6(a)). Next, after applying the current control simplification, as suggested by [7], the GFM is represented by a current source (Fig. 6(b)). Finally, Fig. 6(c) presents the dynamic block diagram of the entire system, linearized around an operating point. Here, the network is modeled as a single-axis dynamic $RL$ segment, given in (5).

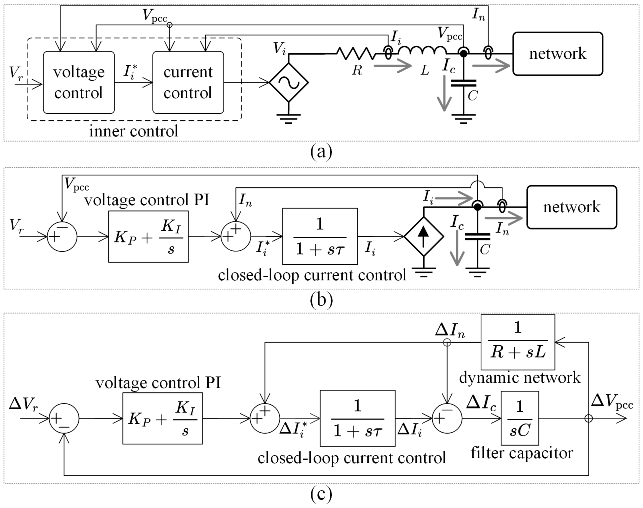


Fig. 6. GFM simplification: (a) GFM as a voltage source with inner control regulating only the voltage at the PCC; (b) simplification of current control resulting in a current source representation of GFM; (c) dynamic block diagram linearized around an operating point with first-order network model.

The GFM output voltage $\Delta V_{pcc}$ appears across the filter capacitor $C$, while the network determines the line current $\Delta I_n$. The closed-loop transfer function of the system shown in Fig. 6 is given by:

$$\frac{\Delta V_{pcc}}{\Delta V_r} = \frac{(R+sL)(K_I+sK_P)}{s^4LC\tau + s^3(LC+\tau RC) + s^2(RC+\tau+LK_P)} \times \frac{1}{+s(RK_P+LK_I)+RK_I} \tag{7}$$

From (7), the impact of all six parameters ($K_P$, $K_I$, $\tau$, $R$, $L$, and $C$) on the system roots can be measured. Under typical normalized GFM parameters (see Table I), the coefficients of $s^4$ and $s^3$ are too small, indicating much faster response and hence can be ignored. Moreover, dividing numerator and denominator with the coefficient of $s^2$ repackages the denominator into the standard form of second order system with the following characteristic equation:

$$s^2 + \left(\frac{RK_P+LK_I}{RC+\tau+LK_P}\right)s + \left(\frac{RK_I}{RC+\tau+LK_P}\right) = 0 \tag{8}$$

Matching the coefficients of (8) with the standard second-order transfer function yields following expressions for the natural oscillation frequency $\omega_n$ and damping ratio $\zeta$.

$$\omega_n = \sqrt{RK_I/(RC+\tau+LK_P)} \tag{9}$$

$$\zeta = \frac{LK_I+RK_P}{2\sqrt{R^2CK_I+\tau RK_I+RLK_PK_I}} \tag{10}$$

The network strength is generally characterized by SCR (denoted by $\mathcal{S}$), and $X/R$ (denoted by $\mathcal{X}$), instead of $R$, and $L$, with $R = 1/(\mathcal{S}\sqrt{1+\mathcal{X}^2})$ and $L = \mathcal{X}/(\omega_0\mathcal{S}\sqrt{1+\mathcal{X}^2})$ at rated power of 1.0 pu. Substituting $R$ and $L$ in (9) gives:

$$\zeta = \frac{\mathcal{X}K_I+\omega_0K_P}{2\omega_0\sqrt{CK_I+\tau K_I\mathcal{S}\sqrt{1+\mathcal{X}^2}+\mathcal{X}K_PK_I/\omega_0}} \tag{11}$$

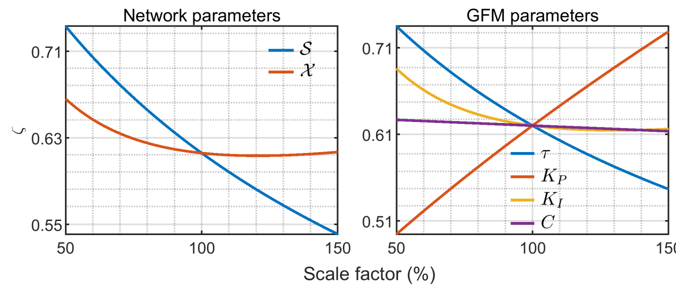


Fig. 7. Damping ratio for varying network parameters (left), and control parameters (right). At base case (100%), $\mathcal{S} = 3$, $\mathcal{X} = 10$, $\omega_0C = 0.22$, $\tau = 0.3$ ms, $K_P = 0.2$, and $K_I = 4.67$.

Sensitivity analysis of $\zeta$ reveals distinct patterns across network and control parameters. The derivatives $\frac{d}{d\mathcal{S}}\zeta$, $\frac{d}{d\tau}\zeta$, and $\frac{d}{dC}\zeta$ are consistently negative, indicating that increases in network strength $\mathcal{S}$, current controller time constant $\tau$, or filter capacitance $C$ reduce system damping. Conversely, $\frac{d}{dK_P}\zeta$ is positive, showing that higher proportional gain $K_P$ enhances damping. The impact of integral gain $K_I$ and network reactance $\mathcal{X}$, represented by $\frac{d}{dK_I}\zeta$ and $\frac{d}{d\mathcal{X}}\zeta$ respectively, is more complex and depends on the relative magnitudes of other system parameters.

These analytical findings are validated in Fig. 7, where parameters are varied around their base values ($\mathcal{S} = 3$, $\mathcal{X} = 10$, $\omega_0C = 0.22$, $\tau = 0.3$ ms, $K_P = 0.2$, and $K_I = 4.67$). Fig. 7 demonstrates the reduction in damping as $\mathcal{S}$ (left) and $\tau$ (right) increase from their base values, while showing improved damping with increased $K_P$ (right).

The analytical insights into parameter sensitivities provide clear understanding of actions conducive in stabilizing GFM-induced oscillations through appropriate selection of control and network parameters.

## V. Validation on a Multi-IBR System

To validate our theoretical findings in a more realistic power system context, we examine a modified two-area 11-bus system [18] incorporating multiple GFMs and GFLs. The test system, shown in Fig. 8, is based on the classical two-area system and features two GFMs and two GFLs. Following [18], the active power loads are modeled as constant current, reactive power loads as constant impedance, and the operating conditions are maintained as in the original system. The GFL dynamic model is adapted from [11], with control gains tuned for a closed-loop bandwidth of 10 Hz. For the GFMs, control gains are determined using the SO method. The $K_{P_{dq}}$ of GFM at bus 1 is reduced to one-tenth of its original value.

Under base operating conditions, when a voltage step change is applied to the GFM at bus 1, raising its reference to 1.05 pu at t = 0.1 s, a poorly damped SSO at approximately 12 Hz is observed in the terminal voltage responses (red traces in Fig. 9). Consistent with our analysis, these SSO can be mitigated through three approaches (blue traces in Fig. 9). These approaches include increasing $K_{P_{dq}}$ to 0.2 from 0.1, reducing $\tau_c$ to 0.2 ms from 0.3 ms, or reducing the network strength by removing one tie line between buses 7 and 9.

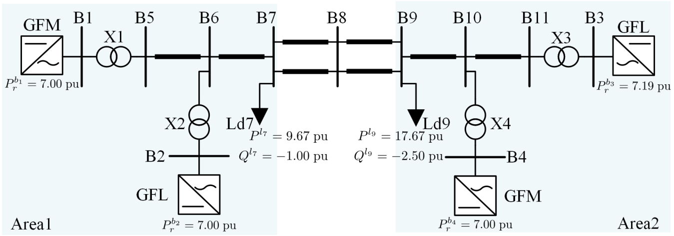


Fig. 8. 11-bus test system with two GFMs and two GFLs [18].

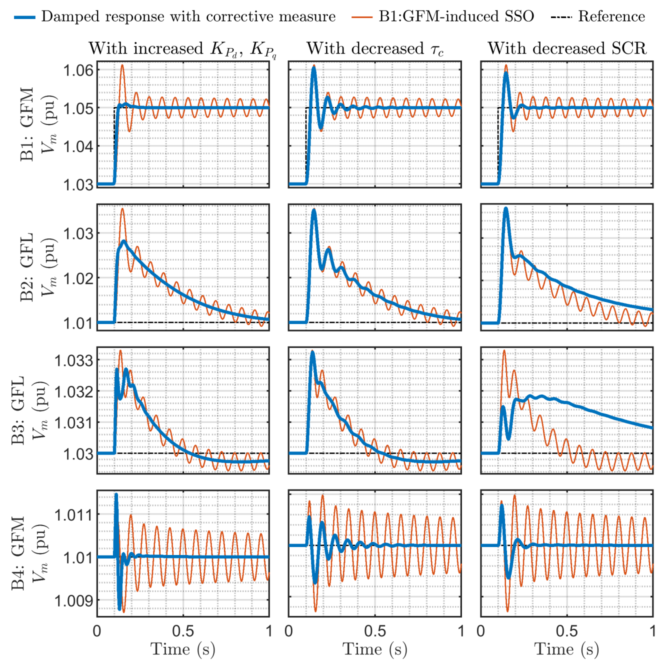


Fig. 9. Dynamic response of terminal voltage of IBR buses for the 11-bus system. The reference voltage of bus 1 is increased to 1.05 pu at 0.1 s.

The effectiveness of these mitigation strategies demonstrates the strong relationship between controller parameters, network configuration, and system stability.

While this study primarily focuses on the interaction between GFM's inner control and network dynamics, inter-GFM oscillations may emerge in systems where GFMs are electrically close and operate with similar bandwidths, This interaction requires further investigation which is one of the areas of our ongoing research.

## VI. Conclusion

This work presents the analysis of GFM-induced subsynchronous oscillations (SSO), revealing that different parameter variations—SCR, voltage control gain, or current control bandwidth—lead to similar oscillatory patterns in terms of participation factors and mode shapes. This similarity makes it challenging to precisely diagnose the sources of oscillations using modal analysis alone. However, it reveals fundamental relationships between GFM control and network states. The analytical findings, validated on a multi-inverter test system, demonstrate that SSO can be effectively mitigated by increasing voltage control gain or current control bandwidth, or by reducing network strength. However, the practical implementation of these solutions must carefully balance SSO mitigation against other operational constraints. Given the increasing volatility in renewables-dominated power systems, we recommend incorporating network strength (perhaps worst-case strength or robust design on uncertain Thévenin equivalent parameters) directly into the GFM control design process, moving beyond traditional localized design approaches to ensure robust stability across various operating conditions.

## References


[1] P. Pourbeik, J. J. Sanchez-Gasca, J. Senthil, J. D. Weber, P. Zadkhast, Y. Kazachkov, S. Tacke, J. Wen, and A. Ellis, "Generic dynamic models for modeling wind power plants and other renewable technologies in large-scale power system studies," *IEEE Transactions on Energy Conversion*, vol. 32, no. 3, pp. 1108–1116, 2017.

[2] Z.-X. Zou and M. Liserre, "Modeling phase-locked loop-based synchronization in grid-interfaced converters," *IEEE Transactions on Energy Conversion*, vol. 35, no. 1, pp. 394–404, 2020.

[3] D. B. Rathnayake, M. Akrami, C. Phurailatpam, S. P. Me, S. Hadavi, G. Jayasinghe, S. Zabihi, and B. Bahrani, "Grid forming inverter modeling, control, and applications," *IEEE Access*, vol. 9, 2021.

[4] P. Sun, J. Yao, Y. Zhao, X. Fang, and J. Cao, "Stability assessment and damping optimization control of multiple grid-connected virtual synchronous generators," *IEEE Transactions on Energy Conversion*, vol. 36, no. 4, pp. 3555–3567, 2021.

[5] M. Chandorkar, D. Divan, and R. Adapa, "Control of parallel connected inverters in standalone ac supply systems," *IEEE Transactions on Industry Applications*, vol. 29, no. 1, pp. 136–143, 1993.

[6] M. Guan, W. Pan, J. Zhang, Q. Hao, J. Cheng, and X. Zheng, "Synchronous generator emulation control strategy for voltage source converter (vsc) stations," *IEEE Transactions on Power Systems*, vol. 30, no. 6, pp. 3093–3101, 2015.

[7] A. Yazdani and R. Iravani, *Voltage-sourced converters in power systems : modeling, control, and applications*. IEEE Press/John Wiley, 2010.

[8] S. D'Arco, J. A. Suul, and O. B. Fosso, "Automatic tuning of cascaded controllers for power converters using eigenvalue parametric sensitivities," *IEEE Transactions on Industry Applications*, vol. 51, no. 2, 2015.

[9] J. Xu, S. Xie, and T. Tang, "Improved control strategy with grid-voltage feedforward for lcl-filter-based inverter connected to weak grid," *IET Power Electronics*, vol. 7, no. 10, pp. 2660–2671, 2014.

[10] Z. Qu, J. C.-H. Peng, H. Yang, and D. Srinivasan, "Modeling and analysis of inner controls effects on damping and synchronizing torque components in vsg-controlled converter," *IEEE Transactions on Energy Conversion*, vol. 36, no. 1, pp. 488–499, 2021.

[11] J. Vochoska, M. S. Javaid, Z. Akhtar, and B. Chaudhuri, "Small-signal stability of power systems with a mix of synchronous generators and inverter-based resources," in *2023 IEEE PES Innovative Smart Grid Technologies Europe (ISGT EUROPE)*, 2023, pp. 1–6.

[12] L. Ding, X. Lu, and J. Tan, "Comparative small-signal stability analysis of grid-forming and grid-following inverters in low-inertia power systems," in *IECON 2021 – 47th Annual Conference of the IEEE Industrial Electronics Society*, 2021, pp. 1–6.

[13] Q. Jia, G. Yan, Y. Cai, Y. Li, and J. Zhang, "Small-signal stability analysis of photovoltaic generation connected to weak ac grid," *Journal of Modern Power Systems and Clean Energy*, vol. 7, no. 2, p. 254, 2019.

[14] L. Gnärig, R. Weiß, A. Hoffmann, and S. Bernet, "Efficient control parameter improvements for inverter-based island grids by means of eigenvalue analysis," in *2023 25th European Conference on Power Electronics and Applications (EPE'23 ECCE Europe)*, 2023, pp. 1–8.

[15] Y. Liu, X. Chen, Z. Chen, X. Shi, L. Lin, and Z. Wang, "Research on the effects of grid-forming control on islanding detection effectiveness of distributed energy resources," in *2023 IEEE 2nd International Power Electronics and Application Symposium (PEAS)*, 2023, pp. 1592–1598.

[16] U. Markovic, O. Stanojev, P. Aristidou, E. Vrettos, D. Callaway, and G. Hug, "Understanding small-signal stability of low-inertia systems," *IEEE Transactions on Power Systems*, vol. 36, no. 5, p. 3997, 2021.

[17] M. H. Ravanji, D. B. Rathnayake, M. Z. Mansour, and B. Bahrani, "Impact of voltage-loop feedforward terms on the stability of grid-forming inverters and remedial actions," *IEEE Transactions on Energy Conversion*, vol. 38, no. 3, pp. 1554–1565, 2023.

[18] P. Kundur, N. Balu, and M. Lauby, *Power System Stability and Control*, ser. EPRI power system engr. series. McGraw-Hill, 1994, pp. 813–814.